Examination of binary alloy free dendritic growth theories with a phase-field model

J.C. Ramirez, C. Beckermann *

Department of Mechanical and Industrial Engineering, The University of Iowa, Iowa City, IA 52242, USA

Abstract

Two-dimensional phase-field simulations are used to test standard theories for free dendritic growth of alloys. While the transport of heat and solute in the melt is predicted well by the theories, the selection criterion for the operating state of the dendrite tip is found to break down in several respects. The selection parameter, σ^*, computed from the phase-field simulations varies strongly with alloy composition, Lewis number, and imposed undercooling, whereas the theories assume σ^* to be independent of these parameters. While the computed σ^* is the same for purely thermal and solutal dendrites, it experiences a minimum at a small but finite solute concentration where thermal and solutal effects are both important. A pronounced growth velocity maximum at this composition is therefore not found in the simulations. The high Péclet number corrections of the LKT theory are found to be ineffective for the present range of undercoolings.

© 2004 Acta Materialia Inc. Published by Elsevier Ltd. All rights reserved.

Keywords: Dendritic growth; Phase-field models; Solidification; Alloys; Simulation

1. Introduction

The free growth of a single dendrite into an undercooled melt is not only one of the most fundamental problems in solidification science, but is also of great relevance as a precursor to the more complex solidification phenomena occurring in metal casting [1–3]. Dendritic pattern formation is generally characterized by a complex interplay of heat/solute diffusion processes and interface curvature effects that are all occurring on different length scales. In free growth, the latent heat and the solute (in the case of an alloy) are both rejected into a uniformly undercooled liquid surrounding the growing dendrite. Although free dendritic growth appears to be well understood in many respects [1,2], its direct numer-

ical simulation still represents a major challenge, even in two dimensions. If successful, however, such numerical simulation offers the possibility of testing existing dendritic growth theories for much larger parameter ranges than would be possible in experiments.

There exist two important limiting cases in free dendritic growth. For pure substances, the growth is limited by the diffusion of heat in the liquid only (purely thermal growth) (e.g. [4–7]). On the other hand, for concentrated alloys the large ratio of the thermal to the solutal diffusivities (of the order of 100–10^4) makes it often possible to assume that the growth occurs isothermally. Then, solute diffusion solely controls the growth (purely solutal growth) (e.g. [8–10]). This work is concerned with the more general case where heat and solute diffusion simultaneously limit the growth. Such thermosolutal growth is important in solidification of relatively dilute binary alloys, even though the thermal diffusivity may be much larger than the solutal diffusivity. Two interesting effects arise during free dendritic growth when

---
* Corresponding author. Tel.: +1 319 335 5681; fax: +1 319 335 5669.

E-mail address: becker@engineering.uiowa.edu (C. Beckermann).

increasing the solute content from zero. Small solute additions tend to destabilize the dendrite tip, which reduces the radius of curvature of the tip and thus increases the tip growth velocity. Upon further solute addition, the growth becomes increasingly controlled by solute diffusion, which tends to reduce the tip velocity due to the much slower diffusion rate of the solute relative to heat. The result of these two competing effects is a pronounced maximum in the tip velocity at small but finite solute concentrations that has been observed in experiments [11]. The theoretical models due to Lipton, Glicksman and Kurz (LGK) [12,13] or Lipton, Kurz and Trivedi (LKT) [14] are widely employed to predict this phenomenon. These models provide a theory of steady-state free dendritic growth that is valid for any solute concentration, including the transition from purely thermal to purely solutal growth (neglecting solute trapping and kinetic effects). It is the objective of the present study to test these models using direct numerical simulations.

Computational modeling of pattern formation in solidification with coupled heat and solute diffusion has been of long-standing interest [15–17]. However, the numerical simulation of thermosolutal growth of dendrites has only been attempted in the past few years [18–24]. Udaykumar and Mao [18] used a mixed Eulerian–Lagrangian framework that treats the immersed phase boundary as a sharp solid–liquid interface. The spatial discretization is performed with the finite volume method. Special care is required for the treatment of the interface, including the numerical calculation of its velocity and curvature. They show the importance of the effects of non-homogeneous thermal and solutal fields. Beltran-Sanchez and Stefanescu [19] present a cellular automaton (CA) model for free growth of alloy dendrites. They address some of the issues that have typically plagued CA models, the most salient of which is the mesh-dependent non-physical anisotropy. Zhao et al. [20] performed sharp-interface, two-dimensional simulations of thermosolutal dendritic growth. The heat and solute conservation equations are solved using the finite element method. They use an adaptive grid that is very fine near the interface and has increasingly larger elements away from it. This is done in order to resolve the steep gradients associated with the solutal boundary layer. The mesh is adapted at each time step in order to avoid problems associated with excessive deformation of the elements and the consequent degradation of mesh quality.

Only a few studies have been reported in the literature where the phase-field method is used to simulate dendritic growth with coupled heat and solute diffusion, despite the popularity of this method for other dendritic solidification problems [6]. Loginova et al. [21] extended the phase-field model of Warren and Boettinger [8] to thermosolutal dendritic growth, but the numerical results are influenced by abnormally high solute trapping and interface width dependencies. Lan et al. [22] used the model of [21] together with an adaptive finite volume mesh that allows the dendrites to grow without the thermal boundary layer reaching the domain boundaries. However, no solution is proposed to remedy the excessive solute trapping and interface width dependencies. Karma [9] has recently proposed a remedy for the problem of artificially high solute trapping in phase-field models by introducing an anti-trapping current in the solute conservation equation. Lan and Shih [23,24] adopted this anti-trapping current concept for phase-field simulations of non-isothermal dendritic growth of binary alloys with forced convection in the melt. Of all the numerical studies of thermosolutal free dendritic growth reviewed above, only [19] presents some limited comparisons of the results to available theories [12–14].

In this study, the phase-field model recently derived by the present authors and co-workers [25] is used to accurately simulate free dendritic growth with coupled heat and solute diffusion in two dimensions. The model of [25] employs a thin-interface analysis and the anti-trapping current concept to allow interface width independent results to be obtained in the absence of solute trapping and interface kinetic effects. The influence of the relevant physical parameters on the characteristics of thermosolutal free dendritic growth is examined, and a detailed comparison of the results with available theories is presented. The paper is organized as follows. In Section 2, the basic theories of free dendritic growth of alloys are reviewed. Section 3 introduces the phase-field model. Section 4 describes various numerical issues associated with the solution of the model equations, including discretization, nonlinear preconditioning, and convergence studies. In Section 5, numerically predicted steady-state dendrite tip velocities and radii, growth Péclet numbers, and tip selection parameters are compared with the theories. Their dependence on the solute concentration, Lewis number (i.e., the ratio of thermal to solutal liquid diffusivities), and imposed melt undercooling is investigated. The conclusions are summarized in Section 6.

2. Review of free dendritic growth theories

The basic theories of free dendritic growth attempt to predict the steady-state tip velocity V and tip radius ρ of a branchless needle crystal growing into an infinite melt of solute concentration c_∞, that is at a temperature below its equilibrium liquidus temperature by an amount ΔT, known as the imposed total undercooling. The first such theories are due to Langer [26], Lipton, Glicksman and Kurz (LGK) [12,13], and Karma and Langer [27]. Lipton, Kurz and Trivedi (LKT) [14] extended the LGK model to high growth rates and Boett-

inger, Coriell and Trivedi (BCT) [28] extended the LKT model to include solute trapping and kinetic effects. Li and Beckermann [29] added the effects of melt convection to the LGK model using simple correlations for the convective heat and solute transport at the tip. Karma and Kotliar [30] developed a microscopic solvability theory (MST) for alloys, based on boundary layer approximations for the thermal and solutal diffusion fields.

The free dendritic growth theories examined here are two-dimensional versions of the LGK and LKT models, which are closely related. Solute trapping and kinetic effects are not considered. The theories consider thermal and solutal transport at the tip of a parabolic dendrite of a dilute binary alloy with constant partition coefficient k and liquidus line of constant slope m. The total imposed undercooling, ΔT is given by

$$\Delta T = \left(\frac{L}{C_p}\right)\Delta_T + \frac{k\Delta T_0\Delta_C}{1 - (1 - k)\Delta_C} + \frac{\Gamma}{\rho}, \tag{1}$$

where the three terms on the right-hand side represent the thermal, solutal, and capillary contributions to the total undercooling, respectively. In the above equation, L is the latent heat of fusion, C_p is the specific heat of the liquid, $\Delta T_0 = |m|c_\infty(1 - k)/k$ is the equilibrium freezing temperature range corresponding to c_∞, and Γ is the Gibbs–Thomson coefficient. The tip radius is denoted as ρ and corresponds to the radius of curvature at the tip of the parabolic dendrite. Note that for a three-dimensional case, where the dendrite is modeled as a paraboloid of revolution, the capillary contribution to the total undercooling in Eq. (1) would be given by $2\Gamma/\rho$, which is twice the amount in the present two-dimensional case. The dimensionless thermal and solutal undercoolings are defined as

$$\Delta_T = \frac{T^* - T_\infty}{L/C_p} \tag{2}$$

and

$$\Delta_C = \frac{c^* - c_\infty}{(1 - k)c^*}, \tag{3}$$

respectively, where T^* and c^* are the temperature and solute concentration in the liquid at the dendrite tip, respectively. It should be pointed out that T^* and c^* are unknown a priori. In the LGK and LKT models for diffusion-controlled growth, the dimensionless undercoolings are calculated from the Ivantsov solutions for steady-state heat and solute diffusion around a parabolic dendrite, i.e., $\Delta_T = \mathrm{Iv}(Pe)$ and $\Delta_C = \mathrm{Iv}(Le\,Pe)$, where $Pe = V\rho/(2\alpha)$ is the thermal Péclet number, α is the thermal diffusivity of the liquid, $Le = \alpha/D$ is the Lewis number and D is the liquid mass diffusivity. The group $Le\,Pe = V\rho/(2D)$ is also known as the solutal Péclet number, Pe_C. The Ivantsov function

for a two-dimensional parabolic "plate" dendrite was obtained by Horvay and Cahn [31] and is given by

$$\mathrm{Iv}(x) = \sqrt{\pi x}\ \exp(x)\mathrm{erfc}(\sqrt{x}), \tag{4}$$

where erfc( ) is the complementary error function. The Ivantsov function solution assumes an isothermal interface, yet the capillarity effect (i.e., the curvature) varies along the interface, making it non-isothermal. Therefore, the capillarity contribution to the undercooling in Eq. (1) can only be interpreted as a first approximation. Trivedi [32,33] has proposed improved models that account for the non-isothermal nature of the interface. Eq. (1) can be non-dimensionalized by dividing it by the unit undercooling, L/C_p, which yields

$$\Delta = \mathrm{Iv}(Pe) + \frac{Mc_\infty\mathrm{Iv}(LePe)}{1 - (1 - k)\mathrm{Iv}(LePe)} + \Delta_\rho, \tag{5}$$

where $M = -m(1 - k)/(L/C_p)$ is a scaled liquidus slope, $\Delta_\rho = \Gamma C_p/(\rho L) = d_0/\rho$ is the dimensionless capillary undercooling, and d_0 is the capillary length.

Eq. (5) is the transport part of the LGK and LKT models. It is one equation with two unknowns, namely the tip radius and the tip velocity; thus Eq. (5) only fixes the product ρV (i.e., the Péclet number). Closure to the problem is provided by a selection criterion, which can be interpreted as a balance between the destabilizing effects of thermal and solutal gradients and the stabilizing effect of interfacial energy [1]. For the case of no solute diffusion in the solid and equal thermal conductivities in the solid and liquid, the LKT selection criterion can be written as follows:

$$\sigma^* = \frac{d_0}{\rho Pe\left[\xi_T + 2\xi_C Le\left(\frac{k\Delta T_0/(L/C_p)}{1 - (1 - k)\Delta_C}\right)\right]}, \tag{6}$$

where σ^* is a selection parameter that is supposed to be constant for a given alloy system (i.e., a given anisotropy strength) and independent of the Péclet number (i.e., the imposed undercooling), the Lewis number, and the solute concentration [1]. In other words, a single value of the selection parameter can be used for purely thermal and purely solutal growth, as well as for the transition from thermal to solutal growth during which the maximum in the dendrite tip velocity is predicted. The square bracket in the denominator of Eq. (6) consists of two terms representing the effects of thermal and solutal gradients at the tip. The factor of two multiplying the solutal part is absent from the thermal part because of the equal thermal conductivities in the solid and liquid and the vanishing solute diffusivity in the solid [12]. The parameters ξ_T and ξ_C in Eq. (6) are corrections for high Péclet numbers [14] that are simply set to unity in the LGK model. In the LKT model, the corrections are given by:

$$\xi_C = 1 + \frac{2k}{1 - 2k - \sqrt{1 + \frac{1}{\sigma^*(LePe)^2}}} \tag{7}$$

and

$$\xi_T = 1 - \frac{1}{\sqrt{1 + \frac{1}{\sigma^*(Pe)^2}}}. \tag{8}$$

The above dendrite growth theory is used extensively in various models of grain structure development in metal castings [34]. Nonetheless, it is not well validated over the entire ranges of the governing parameters that are relevant in various solidification processes. Li and Beckermann [29] compared the results from the LGK theory (modified to include convection) to the experimental data of Chopra et al. [11] for the transparent alloy system succinonitrile–acetone (SCN–ACE). Even though the measured dendrite tip velocity maximum at small solute concentrations is predicted reasonably well by the theory, a significant scatter in the measured selection parameter σ^* was observed at higher concentrations ($c_\infty \geqslant 0.1$ mol%). This scatter is in obvious disagreement with the theory, since the theory assumes that σ^* is independent of the solute concentration, as noted above. Other attempts to experimentally validate the theory are also inconclusive [1,29]. Therefore, an attempt is made in the present study to validate the LGK/LKT theories using numerical simulation. All simulations employ the same values for the partition coefficient, liquidus slope, and anisotropy strength, while the solute concentration, Lewis number, and imposed undercooling are varied in a parametric study.

3. Phase-field model

The phase-field model employed here allows simulation of microstructural pattern formation in solidification of dilute binary alloys with coupled heat and solute diffusion. It is derived and extensively validated in [25]. The model is valid for substances with equal thermal diffusivities in the solid and liquid phases, and vanishing solutal diffusivity in the solid. All material properties are assumed constant. The model reduces to the sharp-interface equations in a thin interface limit where the width of the diffuse interface is smaller than the radius of curvature of the interface but larger than the real width of a solid–liquid interface, and when kinetic effects are negligible. The model employs the anti-trapping current concept of Karma [9] to recover local equilibrium at the interface and eliminate interface stretching and surface diffusion effects that arise when the solutal diffusivities are unequal in the solid and liquid.

Let ϕ represent the phase field, where $\phi = 1$ in the bulk solid phase and $\phi = -1$ in the bulk liquid phase.

The phase field varies smoothly between these bulk values within the diffuse interface region. The anisotropic and dimensionless forms of the phase-field, species and energy equations, for a vanishing kinetic effect, are given, respectively, by [25]

$$\begin{aligned} [A(\hat{n})]^2 &\left[\frac{1}{Le} + Mc_\infty[1 + (1+k)U] \right] \frac{\partial \phi}{\partial t} \\ &= \phi(1 - \phi^2) - \lambda(1 - \phi^2)^2(\theta + Mc_\infty U) \\ &+ \vec{\nabla} \cdot ([A(\hat{n})]^2 \vec{\nabla}\phi) - \frac{\partial}{\partial x}\left[A(\hat{n})A'(\hat{n})\frac{\partial \phi}{\partial y} \right] \\ &+ \frac{\partial}{\partial y}\left[A(\hat{n})A'(\hat{n})\frac{\partial \phi}{\partial x} \right], \end{aligned} \tag{9}$$

$$\begin{aligned} \frac{1+k}{2}\frac{\partial U}{\partial t} &= \vec{\nabla} \cdot \left(\tilde{D}\frac{1-\phi}{2}\vec{\nabla}U + \vec{j}_{at} \right) \\ &+ \frac{1}{2}\frac{\partial}{\partial t}(\phi[1 + (1-k)U]), \end{aligned} \tag{10}$$

$$\frac{\partial \theta}{\partial t} = (Le\tilde{D})\nabla^2 \theta + \frac{1}{2}\frac{\partial \phi}{\partial t}, \tag{11}$$

where $\hat{n} = -\vec{\nabla}\phi / |\vec{\nabla}\phi|$ is the unit vector normal to the interface, $A(\hat{n}) = 1 + \varepsilon \cos 4\varphi$ is a function that describes the surface energy anisotropy, $\varphi = \arctan(\partial_y\phi/\partial_x\phi)$ is the angle between the direction normal to the interface and the horizontal axis, and ε is a dimensionless parameter that characterizes the anisotropy strength. The anti-trapping current $\vec{j}_{at}$ is given by [9]

$$\vec{j}_{at} = \frac{1}{2\sqrt{2}}[1 + (1-k)U]\frac{\partial \phi}{\partial t}\frac{\vec{\nabla}\phi}{|\vec{\nabla}\phi|}, \tag{12}$$

which is non-zero only inside the diffuse interface region.

The time and length scales used to non-dimensionalize Eqs. (9)–(11) are τ_0 and W_0, which represent a relaxation time and a measure of the interface width, respectively. The dimensionless solute diffusivity is $\tilde{D} = D\tau_0/W_0^2$ and λ is a dimensionless coupling parameter, which is chosen as $\lambda = \tilde{D}/a_2$ to simulate kinetics-free growth ($a_2 = 0.6267$) [25]. The dimensionless temperature and concentration are given, respectively, by

$$\theta = \frac{T - T_m - mc_\infty}{L/C_p}, \tag{13}$$

$$U = \frac{\left(\frac{2c/c_\infty}{1 + k - (1-k)\phi} \right) - 1}{1 - k}, \tag{14}$$

where c is a "mixture" concentration that varies smoothly within the diffuse interface, between the values of the concentration in the bulk liquid and solid phases.

The results from Eqs. (9) to (11) can be related to physical units using the relations $W_0 = d_0\lambda/a_1$ and $\tau_0 = (d_0^2/D)a_2\lambda^3/a_1^2$ which follow from the thin interface analysis of [25]. The coupling constant λ is the only free parameter and the results should be independent of λ

when they are converged. Decreasing λ corresponds to decreasing the diffuse interface width, since $\lambda = a_1 W_0/d_0$.

Note that for the limiting case of a one-dimensional system in equilibrium, Eqs. (10) and (11) give $T = T_m + mc_\infty$, $c = c_\infty$, in the liquid, and $c = kc_\infty$ in the solid. Thus, θ and U are both zero everywhere. Eq. (9) then reduces to $(\partial^2\phi/\partial x^2) + \phi - \phi^3 = 0$. The solution to this equation is the equilibrium phase-field profile, $\phi_0 = -\tanh(x/\sqrt{2})$.

The term $(\theta + Mc_\infty U)$ in Eq. (9) represents the thermosolutal driving force for phase-change. The term $\tilde{D}(1-\phi)/2$ in Eq. (10) interpolates smoothly between the values of the solute diffusivity in the solid and liquid, i.e., zero and $\tilde{D}$, respectively. The latent heat release is given by the term $(\partial\phi/\partial t)/2$ in the energy equation.

The simulations in this paper use nonlinear preconditioning of the phase-field equation as introduced by Glasner [35]. This simple technique allows using grids that are much coarser than those required for reasonable accuracy when solving the non-preconditioned phase-field equation. In essence, nonlinear preconditioning consists of introducing a new variable ψ defined as $\phi = -\tanh(\psi/\sqrt{2})$, which makes ψ a signed distance function to the interface. The above relationship between ψ and ϕ is suggested by the equilibrium phase-field profile. Eq. (9) is first expanded as follows:

$$[A(\hat{n})]^2\left[\frac{1}{Le} + Mc_\infty[1 + (1-k)U]\right]\frac{\partial\phi}{\partial t}$$
$$= \nabla^2\phi + \phi(1-\phi^2) - \lambda(1-\phi^2)^2(\theta + Mc_\infty U)$$
$$+ \varepsilon\cos 4\varphi(2 + \varepsilon\cos 4\varphi)\nabla^2\phi$$
$$- 8\varepsilon\sin 4\varphi(1 + \varepsilon\cos 4\varphi)(\varphi_x\phi_x + \varphi_y\phi_y)$$
$$- 16\varepsilon[\cos 4\varphi + \varepsilon(\cos^2 4\varphi - \sin^2 4\varphi)](\varphi_y\phi_x - \varphi_x\phi_y)$$
(15)

which, in terms of ψ, can be written as:

$$[A(\hat{n})]^2\left[\frac{1}{Le} + Mc_\infty[1 + (1-k)U]\right]\frac{\partial\psi}{\partial t}$$
$$= \nabla^2\psi + \sqrt{2}\phi\,|\nabla\psi|^2 - \sqrt{2}\phi + \lambda\sqrt{2}(\theta + Mc_\infty U)(1-\phi^2)$$
$$+ \varepsilon\cos 4\varphi(2 + \varepsilon\cos 4\varphi)[\nabla^2\psi + \sqrt{2}\phi\,|\nabla\psi|^2]$$
$$- 8\varepsilon\sin 4\varphi(1 + \varepsilon\cos 4\varphi)(\varphi_x\psi_x + \varphi_y\psi_y)$$
$$- 16\varepsilon[\cos 4\varphi + \varepsilon(\cos^2 4\varphi - \sin^2 4\varphi)](\varphi_y\psi_x - \varphi_x\psi_y).$$
(16)

Note that in Eq. (16) the ϕ field is still used, but only as a substitute for $-\tanh(\psi/\sqrt{2})$, since repeatedly calculating this hyperbolic tangent term can slow down computations.

4. Numerical procedures

To model free dendritic growth in two dimensions, Eqs. (10), (11) and (16) are solved numerically using finite difference approximations for the spatial derivatives and explicit discretization of the temporal derivatives. The domain consists of a square box (Fig. 1) initially filled with liquid of concentration c_∞ that is undercooled by an amount ΔT (i.e., the ϕ, U and θ, fields are set to -1, 0 and $\Delta = \Delta T/(L/C_p)$, respectively). A small solid seed, where $\phi = 1$, $U = 0$, and $\theta = 0$, is placed in the lower left corner of the box. The crystal axes are aligned with the coordinate axes as shown in Fig. 1. Taking advantage of symmetry, only one quadrant of a dendrite is computed; thus the initial seed is actually a quarter of a circle. Symmetry boundary conditions are applied for all fields on all boundaries of the domain. Due to anisotropy, the circular seed grows preferentially along the horizontal and vertical axes, developing dendritic arms as time marches on (Fig. 1). The rate of change of the tip position of these arms is defined as the tip velocity. Also, the radius of curvature of the tips is calculated numerically as a function of time (see below). When the tip velocity and radius of curvature do not change appreciably with time, a steady-state regime is achieved.

Fig. 1 shows typical simulation results for a set of parameters provided in the figure. For this simulation, the dimensionless grid spacing is $\Delta x = 0.8$, the dimensionless time step is $\Delta t = 0.003$, and the coupling parameter that dictates the interface width is set to $\lambda = 2$. Phase-field contours are plotted for both the initial time and $t\alpha/d_0 = 280,000$, when the steady state is achieved. The upper and lower boxes in Fig. 1 show the dimensionless temperature and solute concentration distributions, respectively, at $t\alpha/d_0^2 = 280,000$. The variation of the solute concentration within the solid phase represents the predicted microsegregation pattern, since sol-
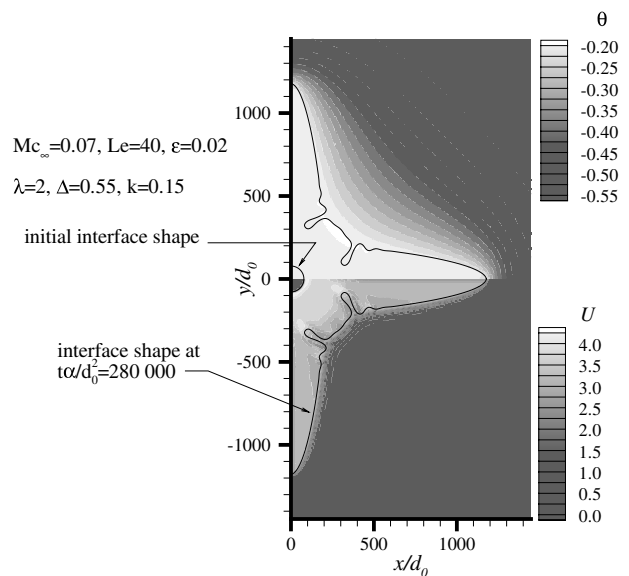

Fig. 1. Typical evolution of the solid/liquid interface shape for an alloy dendrite; the upper and lower boxes show the dimensionless temperature and solute concentration fields, respectively.

ute diffusion in the solid is neglected. It can be seen that for the simulation in Fig. 1 ($Le = 40$) the thermal boundary layer in the liquid is much larger in extent than the solutal boundary layer, which is barely visible. In order to model free dendritic growth into an essentially infinite melt, the domain needs to be large enough that the dendrite can reach a steady growth stage before the thermal boundary layer reaches the far ends of the domain (for $Le \geqslant 1$). Through numerical tests it was determined that as long as the temperature of the rightmost control volume along the lower edge does not increase by more than 0.5% from its initial value, the effect of any wall interaction is negligible.

In order to reduce computational requirements, all simulations are carried out using a non-uniform grid consisting of a square, uniform, fine grid surrounded by a square, uniform coarse grid. The surrounding coarse grid has a grid spacing that is four times larger than the fine grid. The dendrite is always limited in extent to the fine grid, and the coarse grid is primarily used to compute the temperature and solute concentration fields at a sufficiently large distance from the solid/liquid interface where the gradients in these fields are small (note that Fig. 1 shows only the fine-grid region). In the coarse grid region the phase-field is constant ($\phi = -1$, liquid) and the species and energy equations, Eqs. (10) and (11), respectively, reduce to simple unsteady diffusion equations. Eq. (16) for ψ also becomes much simpler in the coarse-grid region due to the vanishing of certain ϕ-dependent terms. The discretized equations for the control volumes where the coarse and fine grids match were carefully derived taking into account continuity of fluxes. It was determined through numerical tests that a ratio of four for the grid spacings generally provides accurate results that are indistinguishable from ones where a fine mesh is used throughout the domain. At the same time, this ratio is large enough that the extent of the coarse mesh region has only a small effect on computational times.

While the total size of the domain is kept constant in a simulation, the fine/coarse mesh set-up is made adaptive. A pre-determined portion of the coarse mesh is refined whenever the dendrite comes close to the boundary of the fine mesh region. In fact, since all simulations in the present study are for relatively high Lewis numbers (10–200), the coarse mesh is already refined when the edge of the solutal boundary layer reaches the boundary of the fine mesh region. Although the fine mesh region increases in size during a simulation, a relatively large coarse grid region remains even at the end of a simulation in order to accommodate the much thicker thermal boundary layer. During a typical simulation, the mesh is adapted approximately five times. An animation of the mesh adaptation during a simulation can be viewed at http://css.engineering.uiowa.edu/~becker/phasefield.htm. It was verified that the mesh adaptation has no effect on

the predicted results by noting that the dendrite tip velocity does not experience any jumps or oscillations in response to a mesh adaptation. Whenever the dimensionless grid spacing is specified in the results below, it refers to the spacing in the fine grid region.

4.1. Calculation of the parabolic dendrite tip radius

Special care is needed for calculating the dendrite tip radius from the computed phase-field contours. The actual radius of curvature at the tip is given by $\rho_a = \partial_x \phi / \partial_y^2 \phi|_{tip}$ [5]. High-order polynomial interpolation is employed for calculating the first and second derivatives of ϕ. The actual tip radius, ρ_a (as well as the tip velocity) is calculated at each time step during a simulation. It is used in the calculation of the solutal undercooling at the dendrite tip, as described in the next subsection.

As shown previously [4,5], ρ_a is not suitable for comparison with dendrite growth theories, because the theories assume a parabolic tip shape. Very close to the tip, the computed dendrite shape differs significantly from a parabola (in two dimensions) due to surface energy anisotropy effects. Therefore, the following procedure is adopted for calculating a parabolic tip radius, ρ, from the computed results at steady state.

If a Cartesian coordinate system (x,z) is placed at the dendrite tip, with z pointing in the direction of growth, the region where the calculated dendrite shape can be approximated by a parabola is that for which the relationship between x_d^2 and z is linear. Here, x_d represents the x-coordinates of the points on the solid/liquid interface. Fig. 2(a) shows a plot of $(x_d/d_0)^2$ vs. z/d_0 for the same dendrite as in Fig. 1 ($t\alpha/d_0^2 = 280,000$). A least squares procedure is employed to determine an equation of the form [4] $(x_d/d_0)^2 = -2\rho[(z/d_0) - z_0]$ that best describes the solid/liquid interface away from the tip. The free parameters obtained through the least squares fitting are the parabolic tip radius ρ and the effective tip location z_0. As shown in Fig. 2, all points on the computational mesh for which z is less than approximately -10ρ are not used in the fit, because the computed dendrite develops secondary structures at larger distances from the tip. The exact end of the fitting range is not important. Furthermore, a certain region near the very dendrite tip is also excluded from the fit due to the non-parabolic nature of the solid/liquid interface there, as noted above. The variation of the parabolic tip radius with the starting point of the fit is shown on the right side of Fig. 2(a). It can be seen that for the example of Fig. 2, the parabolic tip radius is equal to $26.05d_0$ if the fitting range is started at the very dendrite tip (i.e., z/d_0). For a fitting range starting between $50d_0$ ($z \approx -2\rho$) and $120d_0$ ($z \approx -4.6\rho$) from the tip, the parabolic tip radius is on the average equal to $\rho/d_0 \approx 26.1$ and varies by less than 0.2%. Therefore, the beginning of the fitting
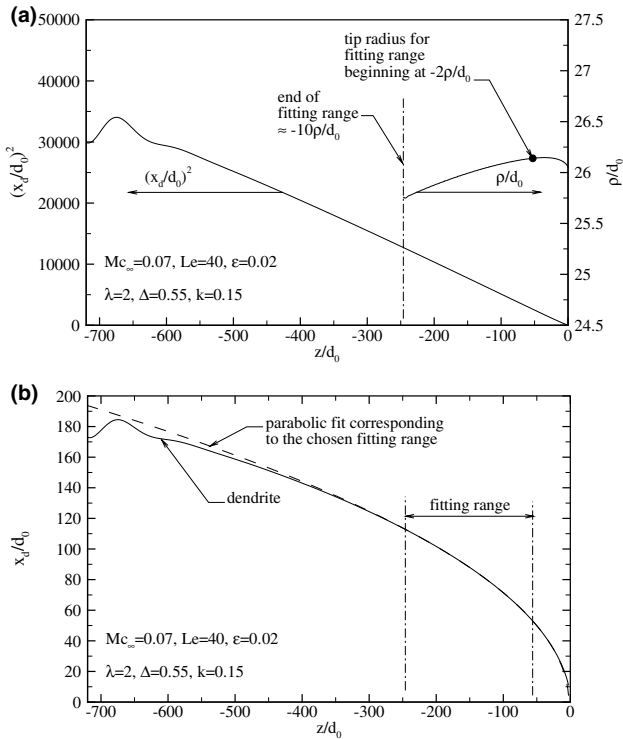
Fig. 2. Determination of the parabolic fit dendrite tip radius: (a) dendrite tip shape in parabolic coordinates, and variation of the tip radius with the beginning of the fitting range behind the tip (the end of the fitting range is always about ten tip radii behind the tip); (b) comparison of the actual dendrite tip shape from the simulation (solid line) with the parabolic fit (dashed line).

range is chosen to be always about two parabolic tip radii away from the tip ($z \approx -2\rho$). This point is indicated as a solid circle in Fig. 2(a). For illustrative purposes, the parabola obtained from the least square fitting procedure is compared to the original dendrite from the phase-field simulation in Fig. 2(b).

4.2. Calculation of the solutal undercooling

In calculating the selection parameter, σ^*, via Eq. (6) using the results of phase-field simulations, it is necessary to know the solutal undercooling at the dendrite tip, Δ_C, in addition to the tip velocity and radius. In the theories, Δ_C is determined from the Ivantsov function solution, i.e., $\Delta_C = \mathrm{Iv}(LePe)$, but this relation cannot be used if the calculated σ^* is intended to be the result of phase-field simulation only. Note that this issue is specific to thermosolutal dendritic growth, because the dendrite tip temperature and solute concentration in the liquid are not known a priori.

Using the definition of U given by Eq. (14), the dimensionless solute concentration at the interface, U_i, can be expressed as $(1 - k)U_i = (c^*/c_\infty) - 1$ [25]. Substituting this relation into Eq. (3), the dimensionless solutal undercooling is given by $\Delta_C = U_i[1 + (1 - k)U_i]$. Hence,

Δ_C can be calculated from the knowledge of U_i. There are two methods for determining U_i from the phase-field results. In the first method, U_i is taken directly from the computed U field as the "frozen-in" value of U in the solid ($\phi \approx 1$) along the dendrite axis right behind the tip (note that U is continuous across the diffuse interface, and that U does not vary in the solid along the dendrite axis during steady growth). In the second method, U_i is determined using the anisotropic Gibbs–Thomson relation, which can be written in dimensionless form as $U_i Mc_\infty = -d_0(\hat{n})\kappa - \theta_i$, where θ_i is the dimensionless interfacial temperature and κ is the local curvature of the interface. When applied in the direction of the horizontal dendrite growth axis, this relation becomes [5]

$$U_i = \frac{-d_0(1 - 15\varepsilon)/\rho_a - \theta_i}{Mc_\infty}. \tag{17}$$

Hence, U_i can be calculated with Eq. (17) by recording the actual dendrite tip radius, ρ_a, and the interface temperature, θ_i, during a simulation. Due to the diffuse nature of the interface in the phase-field method, there is some ambiguity regarding the location within the interface at which θ_i is evaluated. Numerical tests indicate, however, that the uncertainty in the measured Δ_C due to this ambiguity is negligible provided the value of ϕ at which θ_i is evaluated is between 0.85 and 0.95. These relatively high values of ϕ (i.e., close to unity; the value for the bulk solid phase) can be used because the solid is close to isothermal [25]. The two methods for determining U_i from the phase-field results and, ultimately, for calculating the solutal undercooling at the tip, Δ_C, give generally the same result to within a few per cent (see [25] and the following section). Unless otherwise noted, the second method is used in evaluating the selection parameter, σ^*.

4.3. Convergence studies

To determine an adequate dimensionless grid spacing Δx, several simulations are performed varying this parameter only. A solid seed of radius $78d_0$ is used as an initial condition. The other simulation parameters are $\Delta = 0.55$, $Mc_\infty = 0.07$, $Le = 10$, $k = 0.15$ and $\lambda = 2$. For these simulations, the steady-state dendrite tip velocity and parabolic tip radius are determined as previously described and the results are plotted as a function of the grid spacing in Fig. 3. Fig. 3 shows that the tip velocities and radii for the simulations with and without nonlinear preconditioning converge to the same values at small grid spacings ($\Delta x \leqslant 0.3$). However, it is readily apparent that the use of nonlinear preconditioning yields quite accurate results even with grid spacings as large as 1.4. On the other hand, the results without preconditioning rapidly deteriorate with increasing grid spacing, and no converged solution is obtained for $\Delta x > 1.0$. All subsequent simulations are performed with
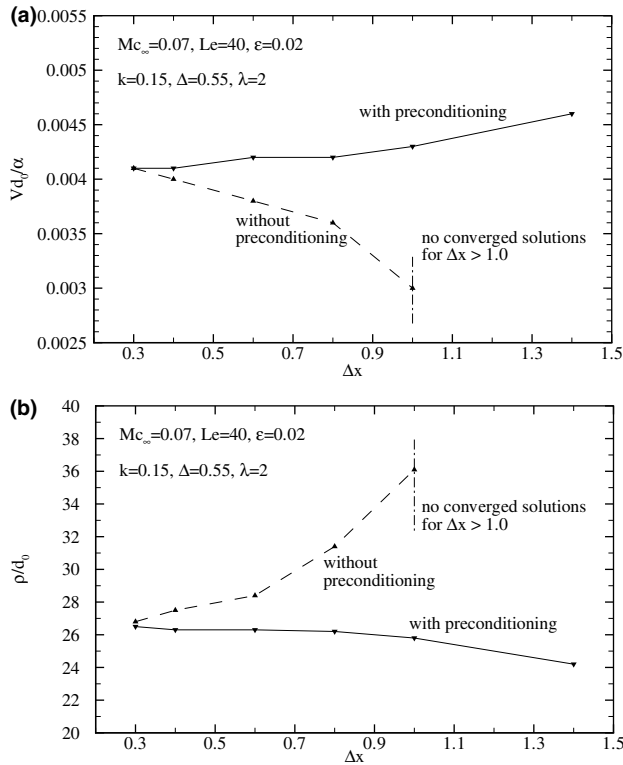
Fig. 3. Convergence behavior of the tip velocity (a) and radius (b) with respect to the dimensionless grid spacing; results are shown for simulations with and without nonlinear preconditioning (solid and dashed lines, respectively).
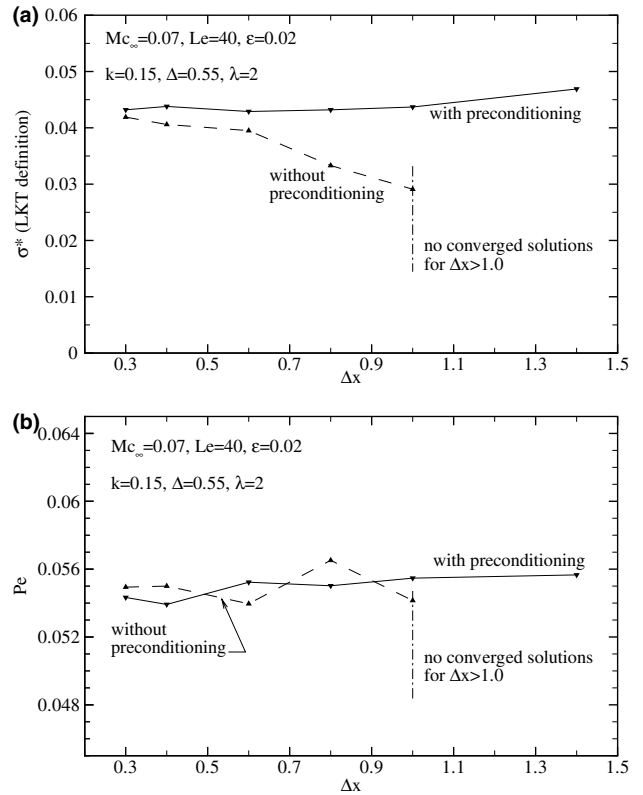

Fig. 4. Convergence behavior of the selection parameter from the LKT definition (a) and the Péclet number (b) with respect to the dimensionless grid spacing; results are shown for simulations with and without nonlinear preconditioning (solid and dashed lines, respectively).

nonlinear preconditioning and a value for the grid spacing of $\Delta x = 0.8$, unless otherwise specified. With the results in Fig. 3, it is possible to estimate the numerical uncertainties associated with this choice of the grid spacing when using nonlinear preconditioning. The tip velocity and radius for $\Delta x = 0.8$ are within 2.5% and 1%, respectively, of the results for $\Delta x = 0.3$, which can be considered converged. Note that using $\Delta x = 0.8$ instead of $\Delta x = 0.3$ reduces computational times by at least one order of magnitude.

Using the steady-state tip velocity and parabolic tip radius from a simulation, the Péclet number, $Pe = V\rho/(2\alpha)$, is calculated. Substituting these parameters, as well the steady-state solutal undercooling at the tip (see the previous subsection), Δ_C, into Eq. (6), the selection parameter, σ^*, is also determined for each simulation. The effect of the grid spacing on σ^* and Pe is shown in Figs. 4(a) and (b), respectively. Only the LKT definition of the selection parameter is shown, but the qualitative behavior for the LGK definition is similar. Again, the results converge to the same values at small grid spacings. While the uncertainty in the selection parameter due to the grid spacing is negligibly small with nonlinear preconditioning (up to about $\Delta x = 1.0$), the result for σ^* without preconditioning for $\Delta x = 0.8$ is more than 20% below the converged value. With nonlinear

preconditioning, the uncertainty in the Péclet number associated with the use of $\Delta x = 0.8$ is less than 1.5%. The convergence behavior of the Péclet number without preconditioning in Fig. 4(b) appears to be reasonable, but this is a fortuitous event because the velocity greatly decreases with increasing Δx while the radius sharply increases, resulting in an almost constant product (i.e., Pe) of the two.

Next, a convergence study is performed where the interface width in the phase-field model is varied. The same physical parameters as in the above grid size convergence study are used. The interface width is controlled by the dimensionless coupling parameter λ, and simulations are performed for values of λ equal to 1, 2, 3, 4, 6 and, 8. Values of $\lambda < 1$ required impractically long times to reach steady state. The calculated steady-state tip velocities and radii as a function of λ are shown in Fig. 5. For the range of values of λ shown in Fig. 5, convergence seems difficult to obtain, but clearly, it is desirable to keep the interface width (and, hence, λ) as small as possible. Fig. 6 shows the calculated steady-state Péclet number and selection parameter as a function of λ. The Péclet number is much less sensitive to the choice of λ, which can again be explained by the
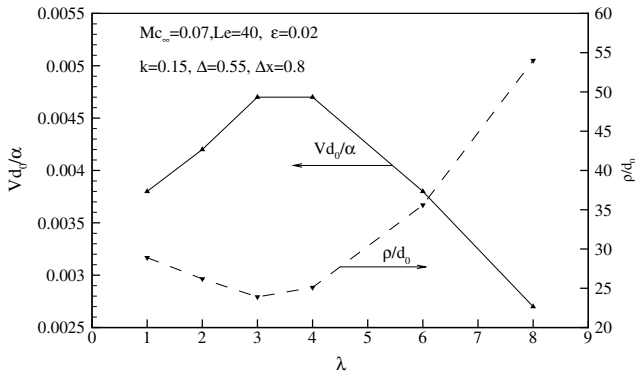
Fig. 5. Convergence behavior of the tip velocity (solid line) and parabolic tip radius (dashed line) with respect to the coupling parameter λ (i.e., the diffuse interface width).
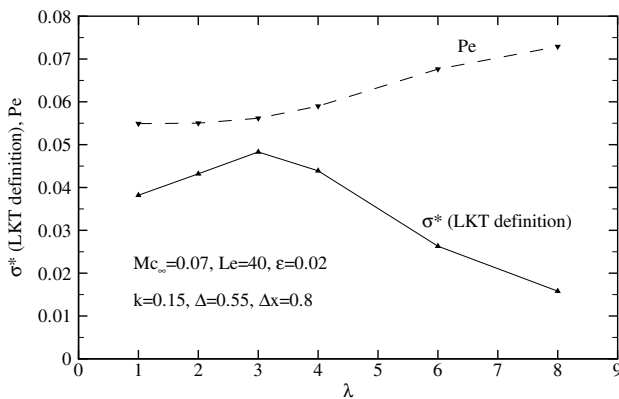

Fig. 6. Convergence behavior of the selection parameter (solid line) and the Péclet number (dashed line) with respect to the coupling parameter λ (i.e., the diffuse interface width).

compensating effect of the tip velocity changing in opposite ways than the tip radius. The selection parameter varies by about 20% for λ between 1 and 4, and rapidly decreases for higher λ. In all subsequent simulations, the coupling parameter is set to $\lambda = 2$, unless otherwise specified. The uncertainty associated with this choice of λ can be estimated by considering the values for $\lambda = 1$ as the most accurate available. Therefore, simulations performed with $\lambda = 2$ predict tip velocities that are within 9% and tip radii that are within 10% of the most accurate values. The uncertainties for Pe and σ^* are less than 0.5% and 10%, respectively.

The total uncertainty in the predicted quantities of interest in the present study can be estimated by taking the root mean square of the uncertainties due to the grid spacing and the interface width. Combining the separate uncertainties in this way, the total uncertainties are approximately 10% for Vd_0/α, 10% for ρ/d_0, 10% for σ^*, and 2% for Pe. These uncertainties are indicated as error bars on the phase-field results in the subsequent comparisons with the theories. While the uncertainties may appear to be rather large, they represent a realistic account of the accuracy that can be achieved with the present phase-field model within a reasonable computational time.

5. Comparison with LGK/LKT theories

5.1. Effect of solute concentration

The phase-field results are first compared to the LGK and LKT theories through a parametric study in which the initial melt composition is varied. The other physical parameters are fixed at $\Delta = 0.55$, $\varepsilon = 0.02$, $k = 0.15$, and $Le = 10$ or $Le = 40$. For these simulations, the choices $\lambda = 2$ and $\Delta x = 0.8$ were adopted.

Figs. 7(a) and (b) show calculated thermal Péclet numbers as a function of initial melt composition for $Le = 10$ and $Le = 40$, respectively. As expected, the Péclet number decreases with increasing solute content. The Péclet numbers predicted by the phase-field simulations are in good agreement with, but slightly below, the LGK/LKT results if the capillary undercooling, $\Delta_\rho = d_0/\rho$, in Eq. (5) is neglected. In that case, the LGK and LKT theories predict the same Péclet numbers.
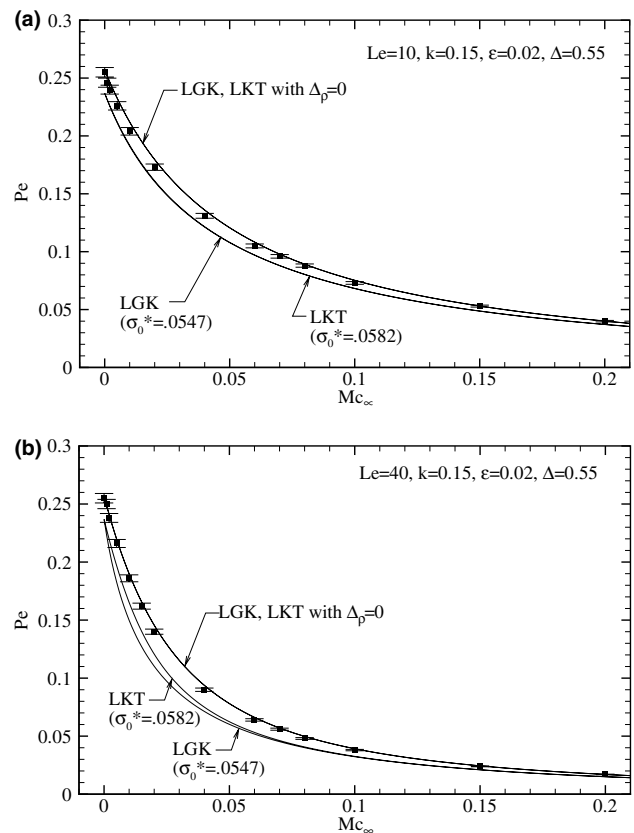

Fig. 7. Comparison between the Péclet number as a function of the initial melt concentration from the phase-field simulations (symbols) and the LGK/LKT theories (lines): (a) $Le = 10$; (b) $Le = 40$.

When the capillary undercooling is not set to zero in the theories, a value for σ^* is needed to determine the tip radius, ρ, from Eq. (6). For that purpose, the ρ and V from the simulation for $Mc_\infty = 0$ (pure substance) were inserted into Eq. (6) and a selection parameter, termed σ_0^*, was calculated. The LGK and LKT theories give σ_0^* that differ by about 6% (0.0547 and 0.0582, respectively). It can be seen from Fig. 7 that the predicted Péclet numbers from the full LGK and LKT theories, including the capillary undercooling, are much lower (by about 10–20%) than the ones for $\Delta_\rho = 0$, and are not in good agreement with the Péclet numbers from the phase-field simulations. Hence, the capillary correction to the undercooling in Eq. (5), $\Delta_\rho = d_0/\rho$, is not accurate, as already noted in Section 2. However, the fact that the Péclet numbers from the simulations are slightly below the theoretical curve for $\Delta_\rho = 0$ indicates that the capillary undercooling is not completely negligible. Nonetheless, the comparison in Fig. 7 confirms the transport part of the LGK/LKT theories for alloys.

Figs. 8 and 9 show the phase-field simulation results (symbols) for the dimensionless tip velocities and radii, respectively, as a function of the initial melt concentration compared to the predictions from the LGK and LKT theories (lines). For the LGK/LKT results, the capillary undercooling is neglected and values for σ^*
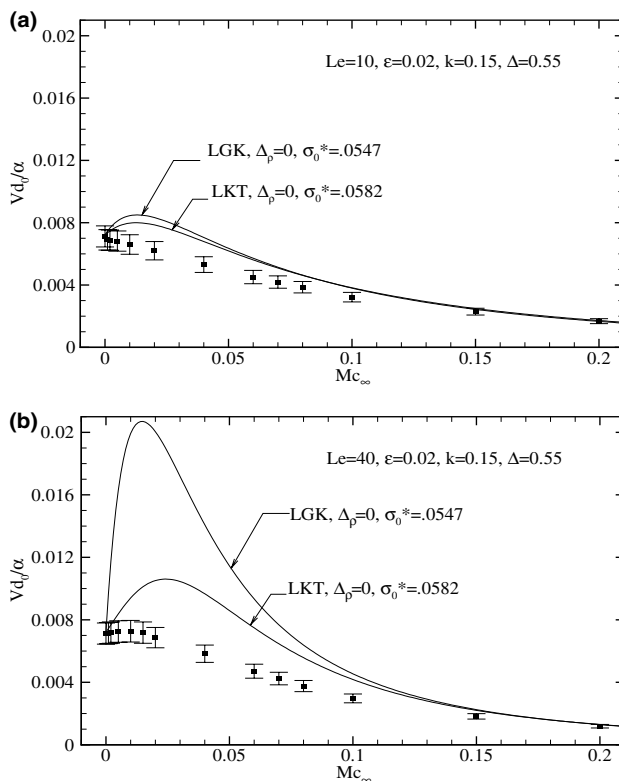

Fig. 8. Comparison between the tip growth velocity as a function of the initial melt concentration from the phase-field simulations (symbols) and the LGK/LKT theories (lines): (a) $Le = 10$; (b) $Le = 40$.
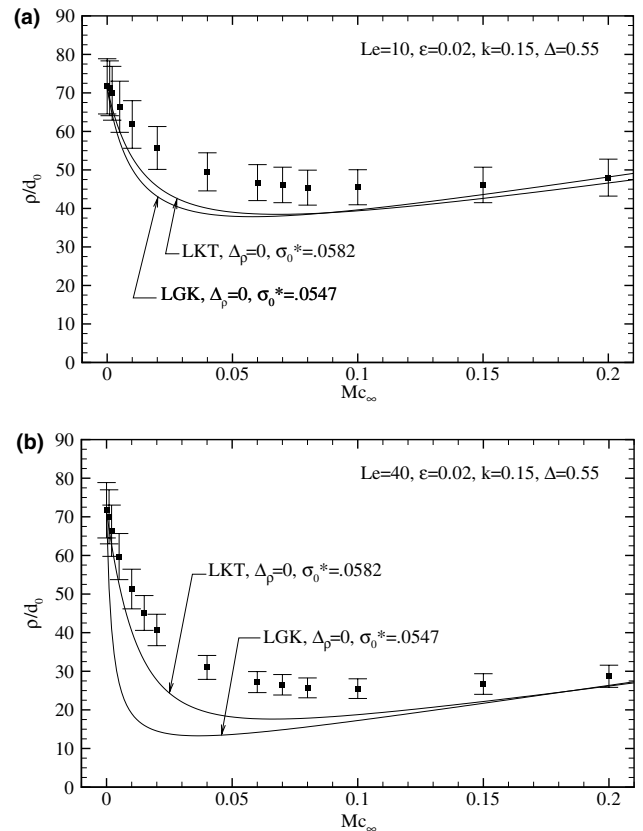

Fig. 9. Comparison between the parabolic tip radius as a function of the initial melt concentration from the phase-field simulations (symbols) and the LGK/LKT theories (lines): (a) $Le = 10$; (b) $Le = 40$.

are used that correspond to $Mc_\infty = 0$, i.e., the same σ_0^* as in Fig. 7. It can be seen that the agreement between the simulation and theory results is excellent for the pure substance case ($Mc_\infty = 0$) and for relatively high concentrations ($Mc_\infty \geqslant 0.15$). However, for $0 < Mc_\infty < 0.15$, which is the range where thermal and solutal effects are both of importance, a large disagreement can be observed. In particular, the pronounced tip velocity maximum predicted by the LGK/LKT theories at small solute concentrations (at $Mc_\infty \approx 0.015$), which becomes stronger with increasing Lewis number, is not seen in the simulation results (Fig. 8). For $Le = 10$ (Fig. 8(a)) the tip velocities from the phase-field simulations continually decrease with increasing solute content. For $Le = 40$ (Fig. 8(b)) the tip velocities from the simulations are approximately constant, or show a slight maximum that is within the uncertainty of the simulations, up to about $Mc_\infty = 0.02$ and then decrease; at the maximum, the tip velocities predicted by the LKT and LGK theories are approximately 50% and 200%, respectively, higher. The tip radii (Fig. 9) from the simulations show a slight minimum at $Mc_\infty \approx 0.1$, but the LGK/LKT theories predict the minimum to be more pronounced and at a smaller solute concentration. Note from Figs. 8 and 9 that the LGK and LKT theories are in relatively close

agreement at all concentrations other than for a certain interval around the tip velocity maximum, where the LKT theory always predicts a smaller maximum than the LGK theory. This indicates that the Péclet number corrections to the selection criterion, Eqs. (7) and (8), play an important role in the prediction of the tip velocity maximum, and that this role becomes increasingly important at higher Lewis numbers.

The above disagreement between the phase-field results and the LGK/LKT predictions can only be explained by a breakdown of the selection criterion, Eq. (6), at solute concentrations near the tip velocity maximum, where the coupling between thermal and solutal effects is most important. Recall that the LGK/LKT theories assume that the selection parameter σ^* is independent of the solute concentration (and the Lewis number). In order to test this assumption, the phase-field simulation results for Vd_0/α, ρ/d_0, and Δ_C are now inserted into Eq. (6) to obtain a calculated σ^*. The results as a function of solute concentration are shown in Figs. 10(a) and (b) for $Le = 10$ and $Le = 40$, respectively. The LGK and LKT theories result in different calculated σ^* because of the Péclet number corrections in the LKT theory; the difference is most significant at solute concentrations near the tip velocity maximum. It can be

seen from Fig. 10 that the σ^* calculated from the phase-field simulations are generally a strong function of the solute concentration, which is in direct contradiction to the LGK/LKT theories. Increasing the solute concentration from zero, σ^* first sharply decreases [especially for $Le = 40$, Fig. 10(b)], reaches a minimum at a concentration near the tip velocity maximum, and then increases to asymptotically approach a constant value for high concentrations. For $Le = 40$, the minimum calculated σ^* is about 60% (35%) below the pure substance value, σ_0^* using the LGK (LKT) definition.

In order to determine the limiting value of σ^* as the solute concentration increases to very large values, an additional simulation was performed for a purely solutal dendrite by assuming that the Lewis number is infinitely large and using a solutal undercooling of $\Delta_C = 0.55$ (with $k = 0.15$, $\varepsilon = 0.02$). As can be seen from Fig. 10, the values obtained for σ^* are 0.0580 and 0.0592 for the LGK and LKT definitions, respectively. These values for a purely solutal dendrite are within about 5% of the σ^* ($= \sigma_0^*$) values for the corresponding purely thermal dendrite (see Fig. 10), which is well within the numerical uncertainty. The good agreement indicates that the selection criterion, Eq. (6), is correct to the extent that the same σ^* can be used for the limiting cases of purely thermal and purely solutal ($Le \to \infty$) dendrites. Note that the thermal and solutal dendrite growth problems are not completely equivalent [see discussion below Eq. (6)]. Therefore, the above agreement in the σ^* values establishes some confidence in the phase-field simulations.

In summary, while the transport part of the LGK/LKT theories (without the capillary undercooling) is well validated by the present simulations, the selection criterion appears to break down at small solute concentrations where thermal and solutal effects are both important and the theories predict a dendrite tip velocity maximum. For the present set of the governing parameters, no pronounced tip velocity maximum is predicted by the phase-field simulations when increasing the solute concentration. The main difference between the simulations in this section and the experiments where the tip velocity maximum was observed [11] is that the dimensionless undercooling, Δ, in the simulations is much higher than that in the experiments. The effect of the imposed undercooling on σ^* is investigated further in Section 5.3.
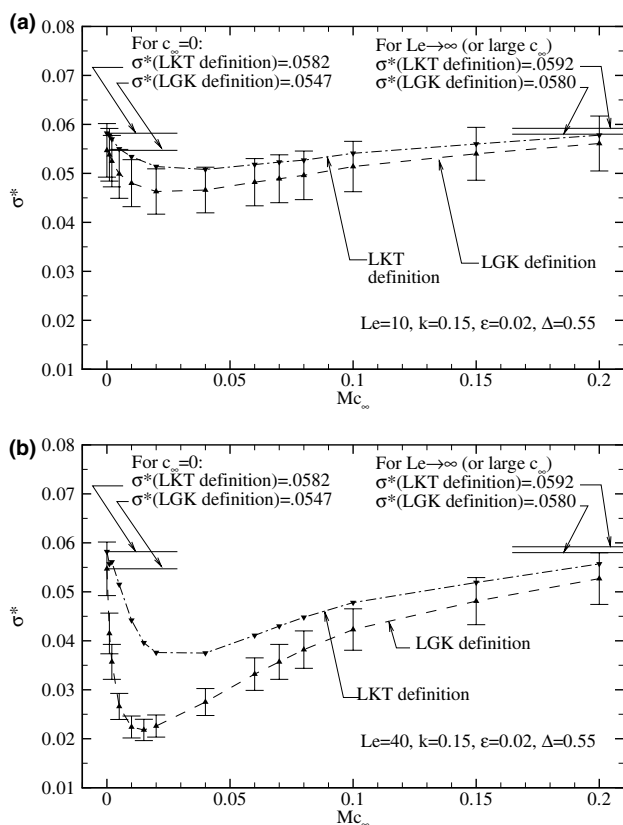

Fig. 10. Variation of the selection parameter (LGK and LKT definitions) from the phase-field simulations with the initial melt concentration: (a) $Le = 10$; (b) $Le = 40$.

5.2. Effect of Lewis number

In this section, the phase-field simulations are compared to the LGK and LKT theories in a parametric study in which the Lewis number is varied from $Le = 1$ to $Le = 200$. The other physical parameters are fixed at $\Delta = 0.55$, $\varepsilon = 0.02$, $k = 0.15$, and $Mc_\infty = 0.01$. The value of $Mc_\infty = 0.01$ was chosen because it is close to the initial

melt concentration where the tip velocity maximum is observed in the theories, the thermal and solutal effects are both important, and the deviation between the simulations and the theories is largest (see Figs. 8–10).

For the simulations in this section, the choices $\lambda = 1$ and $\Delta x = 1.4$ were adopted. The relatively large dimensionless grid spacing is needed to provide a sufficient number of grid points to resolve the large thermal boundary layers associated with the higher Le cases while keeping computational times at a reasonable level. It can be seen from Figs. 3 and 4 that with preconditioning, $\Delta x = 1.4$ still provides reasonably accurate results. The overall uncertainty in the results is considerably reduced by choosing an interface width that is smaller by a factor of two compared to the previous section (i.e., $\lambda = 1$ instead of $\lambda = 2$; see Figs. 5 and 6). The estimated uncertainties are now 10% for tip velocity, 10% for tip radius, 8% for σ^*, and 3% for Pe. An additional convergence check is provided in Table 1. In this table, three parameters are provided as a function of the Lewis number: (i) the ratio of the interface width to the solute diffusion length, $W_0 V/D$, which should be less than unity [25], (ii) the ratio of the actual tip radius to the interface width, ρ_a/W_0, which should be greater than about 10 [25,36], and (iii) the per cent difference between the dimensionless solute concentration, U_i, predicted at the dendrite axis and that calculated from the Gibbs–Thomson condition, Eq. (17). Table 1 shows that except for the simulations with $Le = 150$ and 200, all three parameters are well within ranges that indicate convergence. For $Le = 150$ and 200, $W_0 V/D$ slightly exceeds unity, but this should not be a source of great concern.

Fig. 11 shows a comparison of the Péclet numbers calculated from the phase-field simulations and the LGK/LKT theories as a function of Le. As in Fig. 7, good agreement is observed with the theories when the
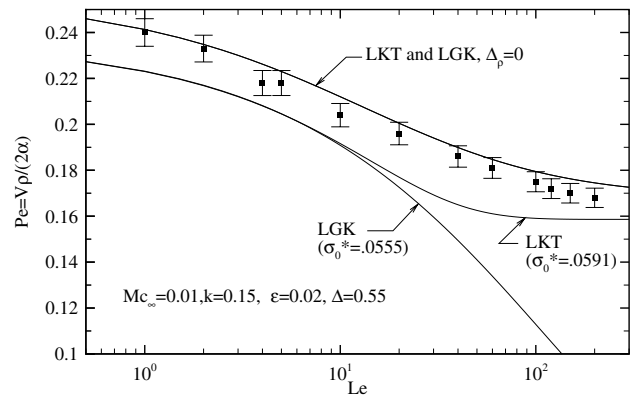

Fig. 11. Comparison between the Péclet number as a function of the Lewis number from the phase-field simulations (symbols) and the LGK/LKT theories (lines).

capillary undercooling in Eq. (5) is neglected. The theoretical curves that include the capillary undercooling are much below the phase-field simulation results; in fact, the LGK curve appears to diverge from the simulation results with increasing Le. Note that the σ_0^* values in Fig. 11, used to determine the tip radius in the capillary undercooling, are slightly different from the ones in the previous section (Figs. 7–9). This can be attributed to the use of different values for Δx and λ. However, the difference in the σ_0^* values is less than 1.5%, which is well within the numerical uncertainty. Like Fig. 7, Fig. 11 lends strong support to the transport part of the LGK/LKT theories.

Figs. 12(a) and (b) compare the phase-field results for the dendrite tip velocity and radius, respectively, to the theories (with $\Delta_\rho = 0$) as a function of the Lewis number. It can be seen that within the present range of Le the tip velocities predicted by the phase-field simulations are approximately constant, while the tip radius decreases slightly with increasing Le. There is a hint of a tip velocity maximum, and tip radius minimum, near $Le = 100$, but no definite conclusion can be made. The variations of the tip velocity and radius with Le from the LGK/LKT theories are generally in poor agreement with the phase-field results. The two theories start to diverge from each other at around $Le = 5$, up to which they are in reasonable agreement with each other and the simulations. Beyond that Lewis number, the LGK theory predicts that the tip velocity (radius) increases (decreases) sharply with increasing Le, while the LKT theory predicts a maximum (minimum) in the tip velocity (radius) at about $Le = 30$. As noted above, these variations are not supported by the phase-field results.

The disagreements in Fig. 12 between the simulation and theories indicate a breakdown of the selection criterion, Eq. (6), as the Lewis number is increased from unity. Recall that the LGK/LKT theories assume that σ^* is a constant that is independent of the Lewis number. Fig. 13 shows the selection parameter, σ^*, calcu-

Table 1

Convergence parameters as a function of the Lewis number for simulations with $Mc_\infty = 0.01$, $k = 0.15$, $\Delta = 0.55$, $\varepsilon = 0.02$, $\lambda = 1$, $\Delta x = 1.4$; the last column shows the per cent difference of the solute concentration predicted along the central dendrite axis with respect to the value obtained from the Gibbs–Thomson condition, Eq. (17)

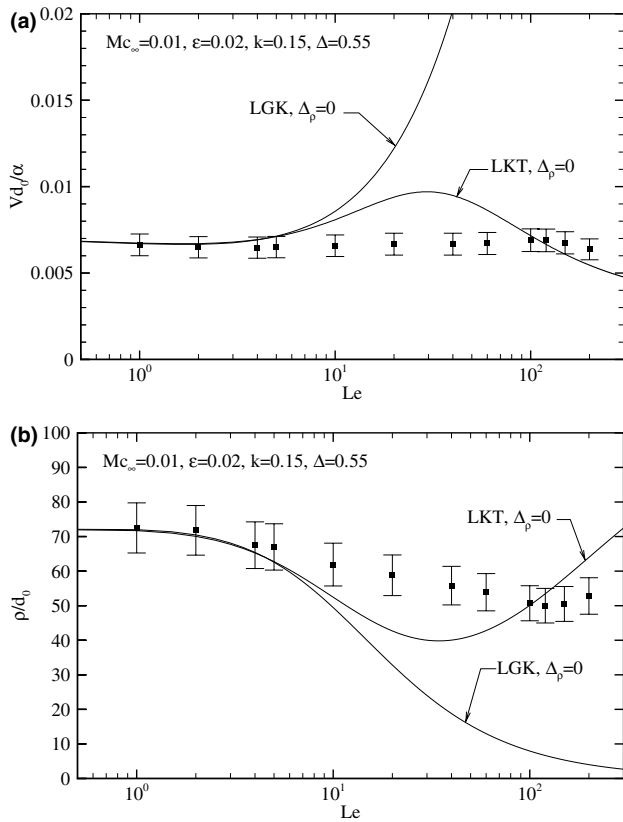| Le	$W_0 V/D$	ρ_a/W_0	% diff. w.r.t. G.T.
1	0.00750	44.4	1.7
2	0.01469	43.8	2.1
4	0.02928	42.1	2.2
6	0.03677	41.2	2.2
10	0.07444	38.1	2.2
20	0.15092	34.6	2.3
40	0.30184	31.3	2.1
60	0.45548	29.0	1.9
100	0.78063	26.0	1.4
120	0.93540	25.3	1.2
150	1.14549	25.0	1.2
200	1.44134	26.1	1.4

Fig. 12. Comparison between the tip growth velocity (a) and the parabolic tip radius (b) as a function of the Lewis number from the phase-field simulations (symbols) and the LGK/LKT theories (lines).

lated from the tip velocities and radii predicted by the phase-field simulations as a function of the Lewis number. Values for both the LGK and the LKT definition of σ^* are provided in the figure. Also indicated in Fig. 13 are the σ^* values for $Le \to \infty$, which were obtained by performing a simulation for purely solutal dendritic growth. Note that the σ^* for $Le \to \infty$ in Fig. 13 are within about 5% of the corresponding values in Fig. 10, the differences being due to the choice
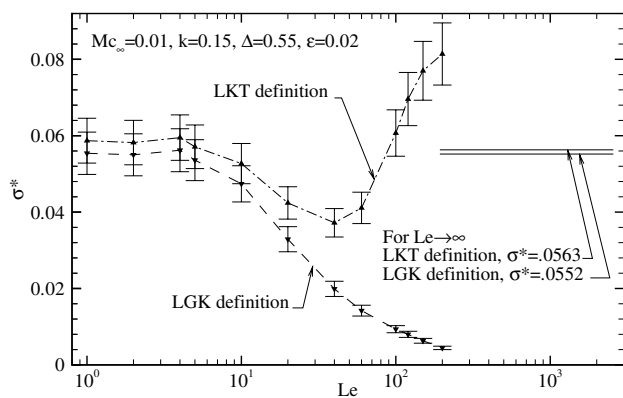

Fig. 13. Variation of the selection parameter (LGK and LKT definitions) from the phase-field simulations with the Lewis number.

of different Δx and λ. It can be seen that for $1 \leqslant Le < 5$, the selection parameters determined from the phase-field simulations are indeed constant and essentially equal to the values computed for $Le \to \infty$. This supports the LGK/LKT theories. However, large variations in the σ^* from the phase-field simulations can be observed for $5 < Le < 200$, which contradicts the theories. For the LGK definition σ^* appears to continually decrease for $Le > 5$, whereas the σ^* based on the LKT definition shows a minimum at $Le \approx 40$ and then increases beyond the $Le \to \infty$ value. Since it was not possible to perform accurate simulations for $Le > 200$, it is unclear how σ^* varies for higher Lewis numbers and ultimately approaches the value for a purely solutal ($Le \to \infty$) dendrite. To the authors' best knowledge, the strong dependence of σ^* on Le shown in Fig. 13 for a (dilute) binary alloy has not been observed before and indicates a breakdown of the LGK/LKT selection criterion.

5.3. Effect of undercooling

Phase-field simulations have also been conducted to explore the effects of the imposed undercooling, Δ, on dendritic growth of an alloy. Here, it is of primary interest to check if the selection parameter, σ^*, varies with the undercooling (or the Péclet number, Pe), since the LGK/LKT theories assume that it does not. While it is well known that σ^* depends on the undercooling for dendritic growth of pure substances (e.g. [5]), this has only been demonstrated for the LGK definition of σ^* (in the limit of $Mc_\infty = 0$). Hence, the simulations in this section will allow for an examination of the high Péclet number corrections of the LKT theory, which are intended to keep σ^* constant as Pe (or Δ) is increased. Furthermore, it is important to verify the LKT corrections for alloys and when thermal and solutal effects are both important.

It is also of interest to examine the limit of small undercoolings (or Pe), where the LGK and LKT theories do not differ. It is essentially in this limit where the tip velocity maximum as a function of the solute concentration has been observed experimentally [11]. Unfortunately, the lowest dimensionless undercooling, Δ, for which it was possible to perform phase-field simulations within a reasonable computational time is equal to 0.1, which is still much above the values in the experiments. In fact, for $\Delta = 0.2$ and $\Delta = 0.1$ the simulations performed in the course of this study did not reach a complete steady growth state. The results are included here because, even though the tip velocity and radius did not reach their steady-state value, the selection parameter had to within the numerical uncertainty. Nonetheless, the simulation results for $\Delta = 0.2$ and $\Delta = 0.1$ should be viewed with caution. Simulations are performed for three cases: (i) purely thermal dendrites

$(Mc_\infty = 0)$, (ii) purely solutal dendrites $(Le \to \infty)$, and (iii) thermosolutal dendrites with $Mc_\infty = 0.01$ and $Le = 40$. The latter case corresponds to the concentration where the tip velocity maximum is expected from the theories and where thermal and solutal effects are both important. Other simulation parameters are held at $k = 0.15$, $\varepsilon = 0.02$, and $\Delta x = 1.4$.

The choice of the coupling parameter, λ, deserves special attention for the low undercooling simulations in this section. The simulations with lower undercoolings can be performed with a much larger λ (and, hence a much larger W_0/d_0) than is necessary for the simulations in the previous sections with $\Delta = 0.55$. This can be attributed to the much lower growth velocities in the simulations with a lower undercooling, which increase the solutal diffusion length, D/V, relative to the interface width. Table 2 provides a list of the same three convergence parameters as in Table 1 for all undercoolings and cases presented in this section. It can be seen that for the present choices of λ, $W_0 V/D < 0.3$, $W_0 V/\alpha < 0.008$, $\rho_0/W_0 > 12$, and the deviation from the Gibbs–Thomson condition is always less than about 3%. Hence, the results can be considered converged with respect to λ (or the interface width) [25,36]. Note that a value of λ as high as 40 can be used for the simulations with $\Delta = 0.1$.

Table 2
Convergence parameters as a function of the imposed undercooling and the coupling parameter λ for purely thermal, purely solutal, and thermosolutal dendritic growth; the last column shows the per cent difference of the solute concentration predicted along the central dendrite axis with respect to the value obtained from the Gibbs–Thomson condition, Eq. (17); the results for $\Delta = 0.2$ $\Delta = 0.1$ are not at a complete steady state

Δ	λ	$W_0 V/D$	ρ_a/W_0	% diff. w.r.t. G.T.
Thermosolutal, $Mc_\infty = 0.01$, $k = 0.15$, $Le = 40$, $\varepsilon = 0.02$				
0.1	40	0.018	17.3	2.2
0.2	10	0.046	21.4	2.3
0.3	8	0.150	12.9	2.8
0.4	2	0.137	66.0	2.3
0.55	1	0.302	31.3	2.1
Δ_C	λ	$W_0 V/D$	ρ_a/W_0	% diff. w.r.t. G.T.
Purely solutal, $k = 0.15$, $\varepsilon = 0.02$				
0.1	40	0.0005	18.9	1.3
0.2	10	0.0018	18.5	1.3
0.3	8	0.0052	12.5	2.3
0.4	2	0.0049	26.5	1.8
0.55	1	0.01549	22.1	3.3
Δ_T	λ	$W_0 V/\alpha$	ρ_a/W_0	% diff. w.r.t. G.T.
Pure substance, $\varepsilon = 0.02$				
0.1	40	0.0005	26.0	N/A
0.2	10	0.0009	27.6	N/A
0.3	8	0.0029	24.2	N/A
0.4	2	0.0026	50.6	N/A
0.55	1	0.0079	44.1	N/A

Fig. 14 shows a comparison of the Péclet numbers from the phase-field simulations with the LGK/LKT theory (with $\Delta_\rho = 0$ only) as a function of the undercooling. The horizontal axis represents the total undercooling Δ for the pure substance and thermosolutal cases, and the solutal undercooling Δ_C for the purely solutal case. Similarly, the vertical axis represents the thermal Péclet number for the pure substance and thermosolutal cases, and the solutal Péclet number for the purely solutal case. Since the $Pe(\Delta)$ relation for the pure substance case is the same as the $Pe_C(\Delta_C)$ relation for the purely solutal case, the theory curves for these two cases overlap. Fig. 14 shows that the simulation results for these two cases (open circles and solid diamonds) agree to within the numerical uncertainty. Overall, there is good agreement between the simulations and the theory for all three cases, lending further support to the transport part of the LGK/LKT theories. The Péclet numbers from the simulations for $\Delta = 0.2$ and $\Delta = 0.1$ are somewhat above the theoretical predictions, which can be attributed to these simulations not having reached a complete steady state (see above).

The selection parameters, σ^*, obtained from the phase-field simulations for all three cases are plotted as a function of the Péclet number in Fig. 15. The Péclet number is chosen as the independent variable instead of the undercooling, in order to directly examine the dependence of σ^* on Pe; the Péclet number is related to the undercooling as explained in connection with Fig. 14. For the purely thermal and thermosolutal cases, the abscissa represents the thermal Péclet number, and for the purely solutal case, the abscissa is the solutal Péclet number. The selection parameters determined using the LGK definition are shown in Fig. 15(a), while the ones from the LKT definition are provided in Fig. 15(b). The following observations can be made with respect to Fig. 15:
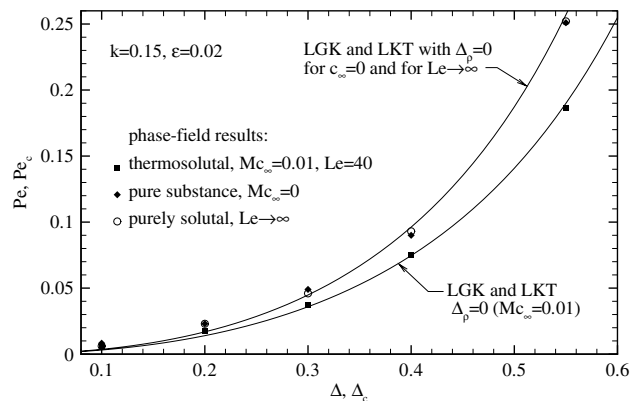

Fig. 14. Comparison between the Péclet number as a function of the imposed undercooling from the phase-field simulations (symbols) and the LGK/LKT theories (lines); for the pure substance and thermosolutal cases, the relationship shown is $Pe(\Delta)$, while for the purely solutal cases, it is $Pe_C(\Delta_C)$.
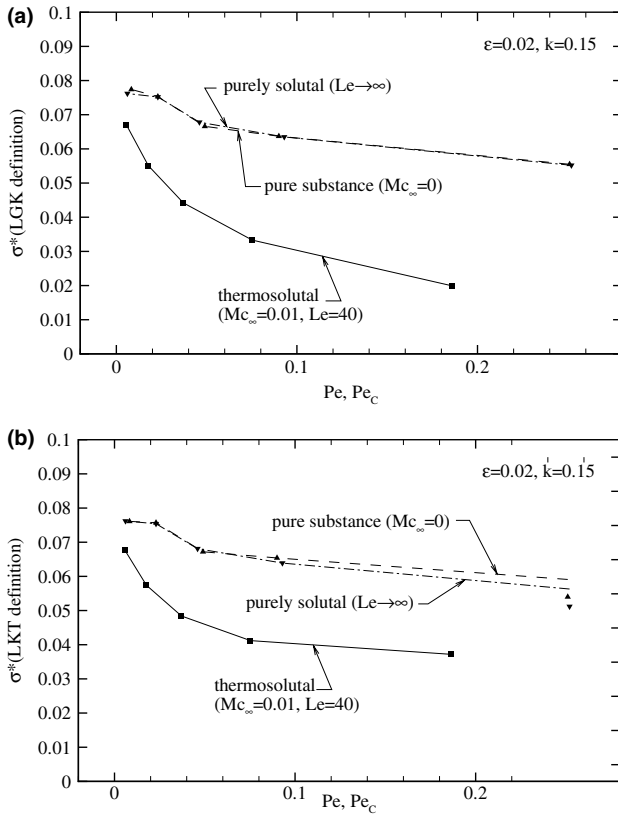
Fig. 15. Variation of the selection parameter from the phase-field simulations, as defined in the LGK (a) and LKT (b) theories, with the Péclet number; the horizontal axis represents the thermal Péclet number for the thermosolutal and pure substance cases, and the solutal Péclet number for the purely solutal case.

- The selection parameters determined from the phase-field simulations are not a constant, but decrease with increasing Péclet number. This indicates a breakdown of the LGK/LKT selection criterion which assume a constant σ^* that is independent of Pe (or the undercooling).
- The high Péclet number corrections in the LKT selection criterion are generally not effective, since the σ^* based on the LKT definition still varies with Pe (Fig. 15(b)). In fact, the differences between the σ^* from the LGK and the LKT definition are relatively minor for $Pe < 0.3$, which is the range examined here.
- As noted in Section 5.1, the selection parameter for the pure substance ($Mc_\infty = 0$) and purely solutal ($Le \to \infty$) cases agree with each other to within the numerical uncertainty. Fig. 15 shows that this is true regardless of Pe, as expected.
- Ignoring the scatter in the σ^* corresponding to $\Delta = 0.2$ and $\Delta = 0.1$ (the two left-most data points), Fig. 15(a) indicates that for the pure substance and purely solutal cases, the selection parameter varies with Pe in an approximately linear fashion, with $\sigma^*(Pe \to 0) \approx 0.07$. Such a linear variation, as opposed

to the nonlinear Pe corrections of the LKT theory, was also found by Karma and Rappel [5] for three-dimensional dendrites of pure substances.

- The selection parameters for the thermosolutal case ($Mc_\infty = 0.01$, $Le = 40$) are much different, and vary more strongly with Pe, than the σ^* in the purely thermal and solutal cases. The solute concentration dependence of σ^* was already noted in connection with Fig. 10. However, Fig. 15(a) shows that the difference between the selection parameters for the thermosolutal case and the ones for the purely thermal and solutal cases becomes less with decreasing Péclet number and that they approach the same value as $Pe \to 0$, i.e., σ^* ($Pe \to 0$) ≈ 0.07 for all three cases. In other words, it is likely that σ^* becomes independent of the solute concentration as $Pe \to 0$. Unfortunately, it was not possible to generate additional numerical data for σ^* in the low Péclet number limit to verify this hypothesis, and even the data corresponding to $\Delta = 0.2$ and $\Delta = 0.1$ in Fig. 15 should be viewed with caution.

The last item may explain why a pronounced dendrite tip velocity maximum as a function of the solute concentration is observed in experiments [11] but not in the simulations (see Fig. 8). The experiments correspond to the low Péclet number limit, whereas the simulations in Fig. 8 are for higher Pe. If indeed the selection parameter is a constant that is independent of the solute concentration as $Pe \to 0$, the maximum in the tip velocity predicted by the LGK/LKT theories is more likely to occur.

6. Conclusions

The standard LGK and LKT theories for free dendritic growth of alloys into an infinite melt (in the absence of kinetic effects and solute trapping) are quantitatively tested using phase-field simulations. The simulations are carried out in two dimensions using a structured adaptive grid and nonlinear preconditioning of the phase-field equation. The uncertainties in the dendrite growth parameters predicted by the simulations are established through extensive convergence studies. Numerous simulations are performed to investigate the effects of the melt concentration, the Lewis number, and the imposed undercooling. It is found that the simulation results for the dendrite tip growth Péclet number are in good agreement with the LGK/LKT theories if the tip radius is based on a parabolic fit to the actual dendrite shape and the capillary undercooling is neglected. However, considerable differences are observed between the simulation results for the dendrite tip velocity and radius and the corresponding LGK/LKT predictions. In particular, the pronounced tip velocity

maximum at a small but finite melt concentration that is predicted by the LGK/LKT theories is not exhibited by the simulation results. These disagreements can be explained by a breakdown of the LGK/LKT selection criterion. The phase-field simulations show that the computed selection parameter, σ^*, based on either the LGK or the LKT definition, varies strongly with initial melt composition, Lewis number and undercooling (or Pe), whereas the theories hinge upon the fact that σ^* is independent of these parameters. While σ^* is the same for purely thermal and purely solutal dendrites, the LGK/LKT selection criterion breaks down at the melt concentration where thermal and solutal effects are both important and the tip velocity maximum is predicted by the theories. The present simulations also show that the high Péclet number corrections of the LKT theory are ineffective for the range of undercoolings investigated here. The results presented in this study should motivate a re-examination of the selection theory for alloys. Additional numerical simulations should be conducted at the low undercoolings where detailed experimental data are available.

Acknowledgments

References

[1] Trivedi R, Kurz W. Int Mater Rev 1994;39:49.
[2] Kurz W, Fisher D. Fundamentals of solidification. 4th ed. TTP; 1998.
[3] Glicksman ME. Mater Sci Eng 1984;65:45.
[4] Tong X. Phys Rev E 63;2001:061601-1.
[5] Karma A, Rappel W-J. Phys Rev E 1998;57:4323.
[6] Boettinger WJ, Warren JA, Beckermann C, Karma A. Annu Rev Mater Res 2002;32:163.
[7] Koss MB et al. Metall Mater Trans A 1999;30:3177.
[8] Warren JA, Boettinger WJ. Acta Metall Mater 1995;43:689.
[9] Karma A. Phys Rev Lett 2001;87:115701.
[10] Jacot A, Rappaz M. Acta Mater 2002;50:1909.
[11] Chopra M et al. Metall Trans A 1988;19:3087.
[12] Lipton J, Glicksman ME, Kurz W. Mater Sci Eng 1984; 65:57.
[13] Lipton J, Glicksman ME, Kurz W. Metall Trans A 1987;18: 341.
[14] Lipton J, Kurz W, Trivedi R. Acta Metall 1987;35:957.
[15] McCartney DG, Hunt JD. Metall Trans A 1984;15:983.
[16] Ungar LH, Bennett MJ, Brown RA. Phys Rev B 1985;31: 5923.
[17] Palle N, Dantzig JA. Metall Mater Trans A 1996;27:707.
[18] Udaykumar HS, Mao L. Int J Heat Mass Transfer 2002;45:4793.
[19] Beltran-Sanchez L, Stefanescu D. Metall Mater Trans A 2003;34:367.
[20] Zhao P, Vénere M, Heinrich J, Poirier D. J Comput Phys 2003;188:434.
[21] Loginova I, Amberg G, Ågren J. Acta Mater 2001;49:573.
[22] Lan CW, Chang YC, Shih CJ. Acta Mater 2003;51:1857.
[23] Lan CW, Shih CJ. J Cryst Growth 2004;264:472.
[24] Lan CW, Shih CJ. Phys Rev E 2004;69:031601.
[25] Ramirez JC, Beckermann C, Karma A, Diepers H-J. Phys Rev E 2004;69:051607.
[26] Langer J. Physicochem Hydrodyn 1980;1:41.
[27] Karma A, Langer J. Phys Rev A 1984;30:3147.
[28] Boettinger WJ, Coriell SR, Trivedi R. In: Mehrabian R, Parrish P, editors. Rapid solidification processing: principles and technologies, vol. 13. Baton Rouge, LA: Claitor's Publishing; 1985.
[29] Li Q, Beckermann C. J Cryst Growth 2002;236:482.
[30] Karma A, Kotliar B. Phys Rev A 1985;31:3266.
[31] Horvay G, Cahn JW. Acta Metall 1961;9:695.
[32] Trivedi R. Scr Metall 1969;3:613.
[33] Trivedi R. Acta Metall 1970;18:287.
[34] Rappaz M. Int Mater Rev 1989;34:93.
[35] Glasner K. J Comput Phys 2001;174:695.
[36] Echebarria B, Folch R, Karma A, Plapp M. arXiv:cond-mat/0404164 2004;2:0404164.